Journal of Materials Chemistry A

Accepted Manuscript

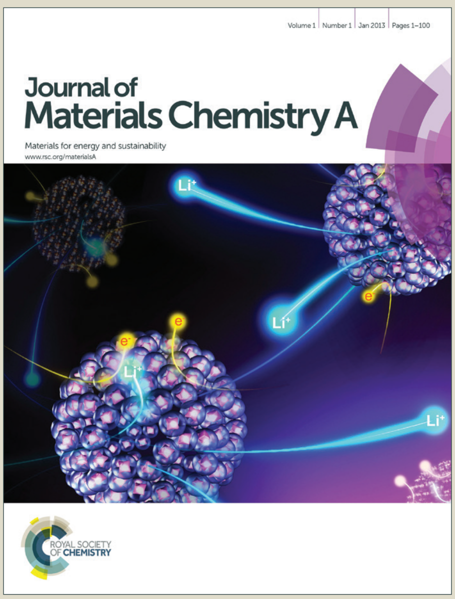

Multiple transition metal oxide mesoporous nanospheres with controllable composition for lithium storage

Zailei Zhang, Qiangqiang Tan,* Yunfa Chen, Jun Yang* and Fabing Su*

State Key Laboratory of Multiphase Complex Systems, Institute of Process Engineering, Chinese Academy of Sciences, Beijing, China 100190,

*To whom correspondence should be addressed. E-mail address: qtan@home.ipe.ac.cn (Q. Tan), Tel.: +86 10 62529377; Fax: +86 10 82545008; jyang@mail.ipe.ac.cn (J. Yang), Tel: +86-10-82544915, Fax: +86-10-82544915; fbsu@mail.ipe.ac.cn (F. Su), Tel.: +86-10-82544850, Fax: +86-10-82544851.

Abstract

A general synthetic method based on a solvothermal route for the preparation of multiple transition metal oxides (MTMOs) mesoporous nanospheres ($Zn_aNi_bMn_cCo_dFe_2O_4$, $0 \leq a, b, c, d \leq 1$, $a + b + c + d = 1$) with controllable composition and uniform size distribution has been developed. The as-prepared $Zn_aNi_bMn_cCo_dFe_2O_4$ nanospheres are formed by self-assembly of nanocrystals with the size of 5–10 nm via structure-directing agents and mineralizer coordinating effect as well as optimization of the synthesis conditions. It has been identified that the addition of mineralizer is crucial for the control of the nucleation process when the metallic precursors are reduced; meanwhile the structure-directing agents is the key to form the mesoporous structure. A number of characterization techniques including X-ray diffraction, transmission electron microscopy, scanning electron microscopy, inductively coupled plasma optical emission spectrometry, temperature-programmed reduction, and nitrogen adsorption have been used to characterize the as-prepared mesoporous products. The overall strategy in this work extends the controllable fabrication of high-quality MTMOs mesoporous nanospheres with designed components and compositions, rendering these nanospheres have promising potential for various applications (oxygen reduction reaction, magnetic performance, supercapacitor, lithium-ion batteries, and catalysis).

1. Introduction

Porous structures have recently gained tremendous interest because of their great potential in various applications such as separation,[1] adsorption,[2] gas sensors,[3] biosensors,[4] optoelectronic applications,[5] drug delivery,[6] catalysis,[7-9] supercapacitors,[10] dye-sensitized solar cells,[11] and lithium-ion batteries.[12-14] In the past decades, there have been great successes on developing effective methods for the synthesis of transition metal oxides (TMOs) including porous CuO microspheres,[15] ZnO layers,[16] CoO nanowires,[17] Co_3O_4 nanosheets,[18] NiO nanowires,[19] alpha-Fe_2O_3,[20] MnO_2 particles,[21] $MnFe_2O_4$ microspheres,[22] spinel $CoFe_2O_4$,[23] $ZnCo_2O_4$ nanotubes,[24] $CoMn_2O_4$ microspheres,[25] $NiCo_2O_4$ nanosheets,[26] and $NiMn_{2-x}Fe_xO_4$.[27] However, most of these reported TMOs porous structures are composed of relatively simple components. In addition, TMOs porous structures with more complexity in terms of structure and element composition are anticipated to offer exciting opportunities for both fundamental studies and practical applications. TMOs, including simple, binary and multicomponents, represent a family of important functional materials which could find widespread uses in magnetic performance,[28, 29] catalyst,[30-34] lithium-ion batteries,[35] and supercapacitors.[36, 37] As an example, binary TMOs are shown to exhibit enhanced lithium storage[38] and supercapacitor performance.[39] Meanwhile, developing strategies to fabricate nanostructures with precisely controlled composition and sizes[40, 41] have attracted considerable research attention owing to their various potential applications.

Recently, designing a general route for controllable synthesis of a series of nanomaterials has become very vital in the view of nanoscience and nanotechnology, because this would provide a great deal of opportunities for studying the relationship between the component/structure and properties of the nanomaterials, as well as a clue to design new types of nanomaterials with desired properties through referring a given method,[42] such as a general strategy for the synthesis of nanocrystals (noble metal, semiconductor, magnetic and dielectric, and rare earth fluorescence nanocrystals),[43] nanoparticles (metal, alloy, semiconductor, core–shell, hollow, and hybrid nanoparticles),[44] few-layer-thick inorganic nanosheets (BN, $NbSe_2$, WSe_2, Sb_2Se_3, and Bi_2Te_3),[45] mesoporous metal oxide microspheres loaded with noble metal nanoparticles (TiO_2/Au, ZrO_2/Au, Al_2O_3/Au, TiO_2/Pd, ZrO_2/Pd, Al_2O_3/Pd, TiO_2/Pt, ZrO_2/Pt, and Al_2O_3/Pt),[46] hollow nanoporous metal oxides (Mn_2O_3, MnO_2, Fe_2O_3, and NiO),[47] hollow and cage-bell nanostructured noble metals (Ru, Rh, Os, Ir, and Pt),[48] rare-earth solid solution colloidal spheres (La, Ce, Y, Gd, Nd, Sm, Er, and Yb oxide),[49] Pt 3d-transition metal nanocubes (Co, Fe, and Ni),[50] metal oxide nanocages (Mn_3O_4, Fe_2O_3, CoO, NiO, ZnO, and Co_3O_4),[42] complex metal oxides tubular nanostructures ($ZnCo_2O_4$, $CoMn_2O_4$, $ZnMn_2O_4$, and $NiCo_2O_4$),[51] multifunctional aqueous nanocrystals (Au, Ag, Pt, Pd, Ag-Au alloy, Ag-Pt alloy, Au-Pt alloy, AgCl, AgBr, CaF_2, NdF_3, SmF_3, Fe_3O_4, $PbCrO_4$, $Sm(OH)_3$, ZnS, CdS, PbS, CuS, and Ag_2S),[52] metal oxide/TiO_2 (Co_3O_4, Fe_2O_3, Fe_3O_4, and CuO) hierarchical heterostructures,[53] ultrathin metal sulphide nanocrystals (CuS nanosheets, ZnS, Bi_2S_3, and Sb_2S_3 nanowires),[54] layered transition-metal nanocones (Ni, $Co_{0.25}$-$Ni_{0.75}$, $Co_{0.5}$-$Ni_{0.5}$, $Co_{0.75}$-$Ni_{0.25}$, $Co_{0.5}$-$Cu_{0.5}$, and $Co_{0.5}$-$Zn_{0.5}$),[55] and multiple-shell metal oxide hollow microspheres (Co_3O_4, NiO, CuO, and ZnO).[56]

These general routes reported so far were mainly focused on synthesizing nano/micro particles with core-shell, porous, and hollow structures that are limited to noble metals, alloys, and metal compounds with simple composition. Therefore the design of a general method with broad applicability for the synthesis of MTMOs porous structures, especially those with compositional accuracy, will attract growing interest and deserve more attention for their low density, excellent loading capacity, and high specific surface area with wide application. Herein, we demonstrate a general controllable synthesis of MTMOs ($Zn_aNi_bMn_cCo_dFe_2O_4$, $0 \le a, b, c, d \le 1$, $a + b + c + d = 1$) mesoporous nanospheres composed of nanocrystals (5–10 nm), which are self-assembled via structure directing agents and mineralizer coordinating effect as well as optimization of the synthesis conditions. This work would be helpful in the fabrication of MTMOs mesoporous structures for potential in various applications (oxygen reduction reaction, magnetic performance, supercapacitor, lithium-ion batteries, and catalysis).

2. Experimental section

2.1 Material synthesis

All the chemicals were of analytical grade and purchased from Sinopharm Chemical Reagent Co., Ltd. Multiple transition metal oxides (MTMOs) mesoporous nanospheres were prepared by a solvothermal method, where the reactant amount, mineralizer, and solvent were varied, and listed in Table 1. In a typical synthesis, for sample $Ni_{0.5}Mn_{0.5}Fe_2O_4$ in entry 22 of Table 1, $Mn(CH_3COO)_2{\cdot}4H_2O$ (0.5 mmol), $Ni(CH_3COO)_2{\cdot}4H_2O$ (0.5 mmol), $FeCl_3{\cdot}6H_2O$ (2.0 mmol), and $CH_3COONa{\cdot}3H_2O$ (18 mmol) were dissolved in $HOCH_2CH_2OH$ (80.0 mL) to form a homogeneous slurry by stirring, which was subsequently sealed in a stainless-steel autoclave and heated at 200 °C for 48 h to obtain the desired products. The resulting precipitate was collected by centrifugation, washed with distilled water and absolute ethanol, and finally dried in vacuum at 80 °C for 24 h.

2.2 Materials Characterization

X-ray diffraction patterns (XRD) were recorded on a PANalytical X'Pert PRO MPD using the Cu Kα radiation of (λ = 1.5418 Å). The microscopic feature of the samples was characterized by field-emission scanning electron microscopy (FESEM) (JSM-7001F, JEOL, Tokyo, Japan) with an analyzer of Energy-dispersive X-ray Spectroscopy (EDX) and transmission electron microscopy (TEM) (JEM-2010F, JEOL, Tokyo, Japan) with EDX. The electron beam was only 2 nm in diameter, capable of providing a high-resolution analysis. The porous property of the samples was investigated using physical adsorption of nitrogen at liquid-nitrogen temperature (–196 °C) on an automatic volumetric sorption analyzer (NOVA3200e, Quantachrome). Prior to the measurement, the sample was degassed at 200 ºC for 24 h under vacuum. The specific surface area was determined according to the Brunauer-Emmett-Teller (BET) method in the relative pressure range of 0.05–0.2. Pore size distribution (PSD) curves were derived from the Barrett-Joyner-Halenda (BJH) method from the adsorption branches. The pore sizes were estimated from the maximum positions of the BJH PSD curves. Temperature programmed reduction (TPR) measurements were carried out on Automated chemisorption analyzer

(ChemBET pulsar TPR/TPD, Quantachrome). Upon loading of 0.10 g of MTMOs mesoporous nanospheres into a quartz U-tube, the sample was degassed at 200 ºC for 30 min under helium. When the temperature dropped to 20 ºC, the gas was changed to 9.9 % H_2/Ar. Finally, the sample was heated from 20 ºC to 800 °C with 10 °C min^{-1} in 9.9 % H_2/Ar with a gas flow of 30 mL min^{-1}. The elemental analysis was conducted by inductively coupled plasma optical emission spectrometry (ICP-OES, Optima 5300DV, Pekin Elmer, USA). Gas Chromatography Mass Spectrometry (GC-MS) (QP2010, SHIMADZU) was employed to calculate the products after reaction.

2.3 Electrochemical Measurement

The working electrode was prepared by mixing the active materials, acetylene black, and polyvinylidene fluoride (PVDF) in a weight ratio of 70:20:10 with N-methylpyrrolidone (NMP) as a solvent. The resulting slurries were cast onto a common Cu foil (current collector). The film composed of Cu foil and slurries were rolled into 25 μm thin sheets, and then dried at 40 ^oC for 24 h. The film were cut into disks with a diameter of 14 mm, and then dried at 120 ^oC under vacuum for 24 h. CR2016 coin-type cells were assembled in an Ar-filled glove box with lithium foils as the counter electrodes and polypropylene microporous films (Celgard 2400) as separators. The liquid electrolyte was 1 mol L^{-1} $LiPF_6$ in a mixture of ethylene carbonate (EC) and dimethyl carbonate (DMC) (1:1, v/v). The galvanostatic charge and discharge tests were carried out by the CT2001A LAND testing instrument in a voltage range between 0.01 and 3.0 V at a current rate of 50 mA g^{-1}. A cyclic voltammogram (CV) was carried out using a CHI660D potentiostat in the voltage range 0−3 V at a scanning rate of 0.1 mV s^{-1} at room temperature.

3. Results and discussion

Our previous studies have demonstrated that the parameters for synthesizing porous structures transition metal oxides (TMOs), such as solvents,[8, 15] mineralizers,[57] and structure directing agents[22, 58] have strong effects on the morphology and pore structure of the products. Therefore, to obtain uniform monodispersed multiple transition metal oxides (MTMOs) mesoporous nanospheres with controllable composition, these parameters were systematically investigated and a formation mechanism of MTMOs mesoporous nanospheres was proposed based on the experimental observations.

3.1. Transition metal oxide nanospheres with mesoporous structures

Fig. 1 shows the SEM images, and TEM images of the ternary TMOs mesoporous nanospheres prepared by adding different metal precursors (entry 10-12 and 22-26 of Table 1). The SEM images show that these ternary TMOs samples including $Zn_{0.5}Co_{0.5}Fe_2O_4$ (Fig. 1a), $Zn_{0.5}Mn_{0.5}Fe_2O_4$ (Fig. 1c), $Zn_{0.5}Ni_{0.5}Fe_2O_4$ (Fig. 1e), $Ni_{0.5}Mn_{0.5}Fe_2O_4$ (Fig. 1g), $Ni_{0.5}Co_{0.5}Fe_2O_4$ (Fig. 1i), and $Mn_{0.5}Co_{0.5}Fe_2O_4$ (Fig. 1k) have uniform spherical morphology with a size distribution of 50–100 nm. We also have investigated the influence of the metal precursor ratio on the composition and morphology of the products. For example, for $Zn_{0.5}Co_{0.5}Fe_2O_4$, the composition of Zn/Co can be tuned by varying the feed ratio between the Zn and Co precursors. Changing the molar ratio of Co/Zn from 1:1 to 1:4 and 4:1, as shown in Fig. S1a and b of Electronic Supplementary Information (ESI), $Zn_{0.2}Co_{0.8}Fe_2O_4$ and $Zn_{0.8}Co_{0.2}Fe_2O_4$ mesoporous nanospheres from ICP-OES analysis (not shown here) were also prepared under the same synthesis condition. The TEM images (Fig. 1b, d, f, h, j, and l) show that these nanospheres have mesoporous structure and each nanosphere is composed of small nanocrystals with the size of 5–10 nm, which serve as the building block units. From the fed molar ratio of metal precursors (Table 1), ICP-OES (not shown here), and SEM-EDX analyses (Fig. S2a, b, c, d, e, and f), the ternary TMOs mesoporous nanospheres of $Zn_{0.2}Co_{0.8}Fe_2O_4$, $Zn_{0.8}Co_{0.2}Fe_2O_4$, $Zn_{0.5}Co_{0.5}Fe_2O_4$, $Zn_{0.5}Mn_{0.5}Fe_2O_4$, $Zn_{0.5}Ni_{0.5}Fe_2O_4$, $Ni_{0.5}Mn_{0.5}Fe_2O_4$, $Ni_{0.5}Co_{0.5}Fe_2O_4$, and $Mn_{0.5}Co_{0.5}Fe_2O_4$ have been accurately prepared.

To further confirm the structure and compositions of these ternary TMOs nanospheres, TEM-EDX and XRD patterns were recorded for all of these samples, which were presented in ESI Fig. S3. TEM-EDX analyses of an arbitrary single nanosphere further reveal the existence of all four elements in the final ternary products, e.g. Zn, Co, Fe, and O for $Zn_{0.5}Co_{0.5}Fe_2O_4$ (ESI Fig. S3a), Zn, Mn, Fe, and O for

$Zn_{0.5}Mn_{0.5}Fe_2O_4$ (ESI Fig. S3c), Zn, Ni, Fe, and O for $Zn_{0.5}Ni_{0.5}Fe_2O_4$ (ESI Fig. S3e), Ni, Mn, Fe, and O for $Ni_{0.5}Mn_{0.5}Fe_2O_4$ (ESI Fig. S3g), Ni, Co, Fe, and O for $Ni_{0.5}Co_{0.5}Fe_2O_4$ (ESI Fig. S3i), and Mn, Co, Fe, and O for $Mn_{0.5}Co_{0.5}Fe_2O_4$ (ESI Fig. S3k). In comparison with the reported data,[59-63] the observed diffraction peaks in the XRD patterns of the as-synthesized ternary TMOs at 2θ of 30.1, 35.6, 43.4, 57.3, and 62.8^o could be indexed to the lattice planes of (220), (311), (400), (511), and (440) respectively, also indicating the formation of $Zn_{0.5}Co_{0.5}Fe_2O_4$[59] (ESI Fig. S3b), $Zn_{0.5}Mn_{0.5}Fe_2O_4$[60] (ESI Fig. S3d), $Zn_{0.5}Ni_{0.5}Fe_2O_4$[61] (ESI Fig. S3f), $Ni_{0.5}Mn_{0.5}Fe_2O_4$[62] (ESI Fig. S3h), $Ni_{0.5}Co_{0.5}Fe_2O_4$[63] (ESI Fig. S3j), and $Mn_{0.5}Co_{0.5}Fe_2O_4$[64] (ESI Fig. S3l).

The hydrogen reduction property, surface areas, and pore sizes of TMOs as functional materials have significant impact on their widespread applications.[8, 57, 65] Herein, we use the $Mn_{0.5}Co_{0.5}Fe_2O_4$ and $Zn_{0.5}Co_{0.5}Fe_2O_4$ nanospheres as examples to examine their H_2-TPR, BET surface areas, and pore size distributions. ESI Fig. S4a shows the H_2-TPR curves of $Mn_{0.5}Co_{0.5}Fe_2O_4$ and $Zn_{0.5}Co_{0.5}Fe_2O_4$. For the $Mn_{0.5}Co_{0.5}Fe_2O_4$, the H_2 consumption peak is located at about 350–650 °C, while for the $Zn_{0.5}Co_{0.5}Fe_2O_4$ nanospheres, a main reduction peak is observed at about 450–650 °C. The maximum reduction peak for $Mn_{0.5}Co_{0.5}Fe_2O_4$ is lower than that of $Zn_{0.5}Co_{0.5}Fe_2O_4$, suggesting $Mn_{0.5}Co_{0.5}Fe_2O_4$ is more reducible. These results demonstrate that the $Mn_{0.5}Co_{0.5}Fe_2O_4$ nanospheres have a higher capability to be reduced than that of $Zn_{0.5}Co_{0.5}Fe_2O_4$, and both of them have relatively low reduction temperature. Nitrogen adsorption measurements (ESI Fig. S4b) show that the BET surface areas of $Zn_{0.5}Co_{0.5}Fe_2O_4$ and $Mn_{0.5}Co_{0.5}Fe_2O_4$ nanopheres are 72.0 and 66.2 m^2 g^{-1} respectively, and their BJH pore size distributions (inset of ESI Fig. S4b), determined from the adsorption branches, at the maxima are 3.1 and 2.6 nm respectively, indicating the presence of mesoporous structure, which originates from the internal space of the nanocrystals, the assembly units for the fabrication of nanospheres. These results demonstrate that the $Mn_{0.5}Co_{0.5}Fe_2O_4$ and $Zn_{0.5}Co_{0.5}Fe_2O_4$ nanospheres have higher surface areas and narrow pore size distributions.

Not surprisingly, quaternary and pentabasic TMOs mesoporous nanospheres can also be obtained simply using this solvothermal method upon the addition of four and five types of metal precursors. A series of quaternary TMOs mesoporous nanospheres have been prepared accordingly (entry 27-33 of Table 1). All of them show a uniform spherical morphology. Importantly, these mesoporous nanospheres can be designed and controllably synthesized with high precision. The molar ratio of each metal element in the final nanospheres can be tuned facilely in accordance to the preset ratio of metal precursors. SEM images of $Zn_{0.33}Ni_{0.33}Mn_{0.33}Fe_2O_4$ (Fig. 2a), $Ni_{0.33}Mn_{0.33}Co_{0.33}Fe_2O_4$ (Fig. 2d), $Zn_{0.33}Mn_{0.33}Co_{0.33}Fe_2O_4$ (Fig. 2g), $Zn_{0.33}Ni_{0.33}Co_{0.33}Fe_2O_4$ (Fig. 2j), and $Zn_{0.25}Ni_{0.25}Mn_{0.25}Co_{0.25}Fe_2O_4$ (Fig. 2m) show that these samples consist uniform nanospheres with the size of 50–100 nm. The compositions of these samples were determined by the fed ratio of metal precursors (Table 1), ICP-OES (not shown here), and the SEM-EDX spectra (Fig. S5a-S5e) analyses. We also have investigated the influence of the metal precursor ratio on the composition and morphology of the products. As an example, for $Zn_{0.33}Ni_{0.33}Mn_{0.33}Fe_2O_4$, the composition of Zn/Ni/Mn can be changed by simply varying the fed ratio between the Zn, Ni, and Mn precursors. Changing the molar ratio of Zn/Ni/Mn from 1:1:1 to 1:2:2 and 2:1:2, the morphology of $Zn_{0.2}Ni_{0.4}Mn_{0.4}Fe_2O_4$ (ESI Fig. S6a) and $Zn_{0.4}Ni_{0.2}Mn_{0.4}Fe_2O_4$ (ESI Fig. S6b) is similar to that of the $Zn_{0.33}Ni_{0.33}Mn_{0.33}Fe_2O_4$ nanospheres at the same preparation condition. The TEM images of these samples (Fig. 2b, e, h, k, and n) show that these nanospheres are mesoporous in structure, and each nanosphere is composed of small nanocrystals with a size of about 5–10 nm. Meanwhile, the HRTEM images of these samples (Fig. 2c, f, i, l, and o) reveal that the lattice fringe spacing is about 0.296 nm. Inset of Fig. 2i and 2o display the discontinuous diffraction rings, suggesting that $Zn_{0.33}Mn_{0.33}Co_{0.33}Fe_2O_4$ and $Zn_{0.25}Ni_{0.25}Mn_{0.25}Co_{0.25}Fe_2O_4$ nanospheres are polycrystalline.

The TEM-EDX analysis of a single nanosphere further reveal the existence of all five elements, e.g. Zn, Ni, Mn, Fe, and O for $Zn_{0.33}Ni_{0.33}Mn_{0.33}Fe_2O_4$ (ESI Fig. S7a), Ni, Mn, Co, Fe, and O for $Ni_{0.33}Mn_{0.33}Co_{0.33}Fe_2O_4$ (ESI Fig. S7c), Zn, Mn, Co, Fe, and O for $Zn_{0.33}Mn_{0.33}Co_{0.33}Fe_2O_4$ (ESI Fig.

S7e), and Zn, Ni, Co, Fe, and O for $Zn_{0.33}Ni_{0.33}Co_{0.33}Fe_2O_4$ (ESI Fig. S7g), and all six elements (Zn, Ni, Mn, Co, Fe, and O) in a single $Zn_{0.25}Ni_{0.25}Mn_{0.25}Co_{0.25}Fe_2O_4$ nanosphere (ESI Fig. S7k). The molar ratio of each element in the final nanosphere is approximately equal to the initial ratio of the metal precursors (Table 1). The diffraction peaks in the XRD patterns at 2θ were observed to be 30.1, 35.6, 43.4, 53.7, 57.3, and 62.8°, respectively, indicating the possible formation of $Zn_{0.33}Ni_{0.33}Mn_{0.33}Fe_2O_4$ (ESI Fig. S7b), $Ni_{0.33}Mn_{0.33}Co_{0.33}Fe_2O_4$ (ESI Fig. S7d), $Zn_{0.33}Mn_{0.33}Co_{0.33}Fe_2O_4$ (ESI Fig. S7f), $Zn_{0.33}Ni_{0.33}Co_{0.33}Fe_2O_4$ (ESI Fig. S7h), $Zn_{0.2}Ni_{0.4}Mn_{0.4}Fe_2O_4$ (ESI Fig. S7i), $Zn_{0.4}Ni_{0.2}Mn_{0.4}Fe_2O_4$ (ESI Fig. S7j), and $Zn_{0.25}Ni_{0.25}Mn_{0.25}Co_{0.25}Fe_2O_4$ nanosphere (ESI Fig. S7l). To our knowledge, the standard XRD patterns of these quaternary and pentabasic TMOs nanospheres were not found from JCPDS cards and reported data because of the scarce researches on these quaternary TMOs.

The STEM image and the corresponding elemental mappings for $Zn_{0.5}Co_{0.5}Fe_2O_4$ nanospheres are displayed in Fig. 3a. As indicated, all elemental components are evenly distributed within the entire nanospheres. The STEM image and elemental mappings of single $Ni_{0.33}Mn_{0.33}Co_{0.33}Fe_2O_4$ mesoporous nanosphere are displayed in Fig. 3b. All elemental components are also evenly distributed within the whole nanosphere. The molar ratio of each element in the final nanospheres is approximately equal to the initial ratio of the metal precursors (Table 1).

3.2. Formation mechanism

The formation mechanism of $Zn_aNi_bMn_cCo_dFe_2O_4$ mesoporous nanospheres is proposed. In the first stage, the Zn^{2+}, Co^{2+}, Ni^{2+}, Mn^{2+}, and Fe^{3+} ions were nucleated under solvothermal conditions via the reaction ($aZn^{2+} + bNi^{2+} + cMn^{2+} + dCo^{2+} + 2Fe^{3+} + 4H_2O + 8CH_3COO^{-} \rightarrow Zn_aNi_bMn_cCo_dFe_2O_4 + 8CH_3COOH$ (from GC-MS analysis)) with the water generated from precursors to form nanosized crystalline $Zn_aNi_bMn_cCo_dFe_2O_4$. When only one of the Zn^{2+}, Co^{2+}, Ni^{2+}, Mn^{2+}, and Fe^{3+} metal ion was added, Fe_2O_3 (ESI Fig. S8a), CoO (ESI Fig. S8b), ZnO (ESI Fig. S8c), NiO (ESI Fig. S8d), and MnO

(ESI Fig. S8e) particles without mesoporous structure were formed (entry 1-5 of Table 1). After addition of Fe^{3+} and the other one metal ions from Zn^{2+}, Co^{2+}, Ni^{2+}, and Mn^{2+}, the larger mesoporous nanospheres of $CoFe_2O_4$ (ESI Fig. S9a), $NiFe_2O_4$ (ESI Fig. S9b), $MnFe_2O_4$ (ESI Fig. S9c), or $ZnFe_2O_4$ (ESI Fig. S9d) with a size of 50–300 nm were obtained accordingly (entry 6-9 of Table 1). With three, four, and five ions were added with Fe^{3+} precursors, the uniform smaller mesoporous nanospheres can be synthesized, as shown in Fig. 1 and 2. In the absence of Fe^{3+} metal precursors, the microparticles, e.g. $Zn_{0.5}Ni_{0.5}Mn_2O_4$ (ESI Fig. S10a) and $Zn_{0.33}Ni_{0.33}Mn_{0.33}Co_2O_4$ (ESI Fig. S10b) (entry 34 and 35 of Table 1), formed under same conditions do not have mesoporous structures. The interaction between Fe^{3+} and other metal precursors might be occurred to promote the self-assembly of nanocrystals for the formation of mesoporous nanospheres. However, the specific interaction between them is yet to be investigated. Meanwhile, the CH_3COONa as a mineralizer plays a crucial role for the formation of $Zn_aNi_bMn_cCo_dFe_2O_4$ mesoporous nanospheres with a narrower size distribution.[57, 58] Using $Zn_{0.5}Co_{0.5}Fe_2O_4$ nanospheres as an example, there were no mesoporous products generated without adding CH_3COONa. However, the more uniform and smaller $Zn_{0.5}Co_{0.5}Fe_2O_4$ nanospheres were formed with the increase of the adding amount of CH_3COONa (50–100 nm with 18 mmol (Fig. 1a), 100–300 nm with 12 mmol (ESI Fig. S11a), 150–500 nm with 9 and 6 mmol (ESI Fig. S11b and S11c), and 300–700 nm with 3 mmol (ESI Fig. S11d)) (entry 12-17 of Table 1). Obviously, the more the added CH_3COONa, the more uniform and smaller nanospheres were formed. However, with further increase of CH_3COONa (such as 21 mmol, not shown here), the size and mesoporous structure is very close to the products obtained in the presence of 18 mmol CH_3COONa. Then, in the second stage, these small nanosized crystalline are self-assembled into large secondary mesoporous nanospheres. $HOCH_2CH_2OH$ can be absorbed on the surface of the nanosized crystalline particles and acted as structure-directing agents to regulate their surface state, influencing the nucleation and aggregate process of the nanoparticles, which are finally assembled to the nanospheres with mesoporous structure.[58] The mesopores are derived from the internal space of these nanocrystals. In the absence or with the decrease of $HOCH_2CH_2OH$, nanoparticles were formed instead of mesoporous nanospheres, as shown in ESI Fig. S12 (entry 18-21 of Table 1). In addition, in the absence of water while keep the presence of $HOCH_2CH_2OH$, the mesoporous nanospheres were formed (Fig. 1b). Increasing the amount of water to 10 and 20 ml, a mixture of the nanospheres and nanoparticles were obtained (ESI Fig. S12a and S12b). Further increasing the water to 30 and 40 ml, the products are mainly composed of nanoparticles (ESI Fig. S12c and S12d). Hence, $HOCH_2CH_2OH$ as structure-directing agent also plays a crucial role for the formation of mesoporous nanospheres.[15]

3.3 Electrochemical Property

Binary[66] and ternary[64] TMOs have been considered as promising electrode materials for lithium-ion batteries. We have therefore investigated the lithium storage properties of the ternary TMOs of $Ni_{0.5}Mn_{0.5}Fe_2O_4$ and quaternary TMOs of $Ni_{0.33}Mn_{0.33}Co_{0.33}Fe_2O_4$ nanospheres. Fig. 4a shows the voltage profiles of $Ni_{0.5}Mn_{0.5}Fe_2O_4$ for the first two cycles at a current density of 50 mA g^{-1}. The discharge and charge capacities in the first run are 1078.2 and 771.4 mAh g^{-1} respectively. These irreversible capacity losses can be attributed mainly to the formation of the solid−electrolyte interface (SEI) layer and the side reactions during the electrochemical process. The initial discharge-charge capacity for these samples might based on the oxidation-reduction reactions of metallic Fe, Ni, and Mn nanoparticles to $Ni_{0.5}Mn_{0.5}Fe_2O_4$: $4Li_2O + 0.5Mn + 0.5Ni + 2Fe \leftrightarrow Ni_{0.5}Mn_{0.5}Fe_2O_4 + 8Li^+ + 8e^-$. A distinct voltage plateau can be clearly identified at ca. 0.8–1.0 V, corresponding to the reduction of Fe^{3+} to Fe, Ni^{2+} to Ni, and Mn^{2+} to Mn during the initial discharge process. Meanwhile, a defined plateau is observed in the charge process at ca. 1.4–2.1 V, corresponding to the oxidation of Fe to Fe^{3+}, Ni to Ni^{2+}, and Mn to Mn^{2+} during the initial charge process. Fig. 4b shows the discharge and charge capacities in the first cycle are 955.3 and 686.0 mAh g^{-1} respectively for $Ni_{0.33}Mn_{0.33}Co_{0.33}Fe_2O_4$ at a current density of 50 mA g^{-1}. Analogously, the irreversible capacity losses can also be attributed mainly to the formation of the SEI layer and the side reactions during the electrochemical process. Little different from those in voltage profiles of $Ni_{0.5}Mn_{0.5}Fe_2O_4$, for $Ni_{0.33}Mn_{0.33}Co_{0.33}Fe_2O_4$, A distinct voltage plateau and defined plateau corresponding to oxidation-reduction reactions of Fe, Co, Ni, and Mn were observed at ca. 0.8–1.0 V and ca. 1.3–2.1 V, respectively. The cycling performance in Fig. 4c shows that the discharge capacity after 60 cycles is about 477.7 mAh g^{-1} for $Ni_{0.5}Mn_{0.5}Fe_2O_4$ and 487.2 mAh g^{-1} for $Ni_{0.33}Mn_{0.33}Co_{0.33}Fe_2O_4$. The coulombic efficiencies of the $Ni_{0.5}Mn_{0.5}Fe_2O_4$ and $Ni_{0.33}Mn_{0.33}Co_{0.33}Fe_2O_4$ electrodes are around 71.5 % and 71.9 %, respectively, in the first cycle. The value quickly increases to around 98.0 % after several cycles, indicating the good reversibility of the electrode. This is because developed mesoporous structure can increase the accommodation of lithium ions and shorten the diffusion distance for lithium ions.[67, 68] So these MTMOs nanospheres present promising potential for the anode materials of lithium-ion batteries. Fig. 4d presents the CV curves of $Ni_{0.5}Mn_{0.5}Fe_2O_4$ nanospheres for the first three cycles at a scan rate of 0.1 mV s^{-1}. In the first scan, one cathodic peak is observed at 0.40–0.85 V, which corresponds to the conversion reactions of Fe^{3+}, Mn^{2+}, and Ni^{2+} to their metallic states and the formation of Li_2O. The broad anodic peak can be ascribed to the oxidation reactions of metallic Fe, Mn, and Ni. The ternary metal oxide $Ni_{0.5}Mn_{0.5}Fe_2O_4$ stores Li through reversible formation and decomposition of Li_2O. In the second scan, the reduction peaks are shifted to 0.55–1.1 V. The asymmetric nature of the plots suggests that the conversion reactions are only partially reversible and the complete structural recovery does not occur. The peak intensity and integral areas of the third cycle decrease with increase of cycling numbers, suggesting that the electrochemical reversibility in the first three cycles is not good.

4. Conclusions

In summary, we have demonstrated a general synthesis of multiple transition metal oxides (MTMOs) mesoporous nanospheres with controllable composition (such as $Zn_{0.5}Co_{0.5}Fe_2O_4$, $Zn_{0.5}Mn_{0.5}Fe_2O_4$, $Zn_{0.5}Ni_{0.5}Fe_2O_4$, $Ni_{0.5}Mn_{0.5}Fe_2O_4$, $Ni_{0.5}Co_{0.5}Fe_2O_4$, $Mn_{0.5}Co_{0.5}Fe_2O_4$, $Ni_{0.33}Mn_{0.33}Co_{0.33}Fe_2O_4$, $Zn_{0.33}Mn_{0.33}Co_{0.33}Fe_2O_4$, $Zn_{0.33}Ni_{0.33}Mn_{0.33}Fe_2O_4$, $Zn_{0.33}Ni_{0.33}Co_{0.33}Fe_2O_4$, and

$Zn_{0.25}Ni_{0.25}Mn_{0.25}Co_{0.25}Fe_2O_4$). The overall strategy presented in this work extends the fabrication of MTMOs mesoporous structures at the nanoscale. We also have demonstrated the promising uses of these MTMOs as negative electrodes for lithium-ion batteries. Meanwhile, these nanospheres may present promising potential for oxygen reduction reaction, magnetic performance, supercapacitor, and catalysis. Also, it should be pointed out that this method is extendable to the preparation of other MTMOs mesoporous nanospheres with different transition metal element composition.

Acknowledgements

The authors gratefully acknowledge the supports from the National Natural Science Foundation of China (No. 51272252, 21031005, and 21376247) and Hundred Talents Program of the Chinese Academy of Sciences.

Electronic Supplementary Information (ESI) available: EDX analyses, H_2-TPR curves, and additional SEM images for the characterizations of the mesoporous nanospheres in this study. See DOI:10.1039/b000000x/

References

1 P. Nugent, Y. Belmabkhout, S. D. Burd, A. J. Cairns, R. Luebke, K. Forrest, T. Pham, S. Q. Ma, B. Space, L. Wojtas, M. Eddaoudi and M. J. Zaworotko, *Nature*, 2013, **495**, 80.

2 M. Hu, J. Reboul, S. Furukawa, N. L. Torad, Q. M. Ji, P. Srinivasu, K. Ariga, S. Kitagawa and Y. Yamauchi, *J. Am. Chem. Soc.*, 2012, **134**, 2864.

3 T. Wagner, S. Haffer, C. Weinberger, D. Klaus and M. Tiemann, *Chem. Soc. Rev.*, 2013, **42**, 4036.

4 H. T. Zhu, J. X. Wang and G. Y. Xu, *Cryst. Growth Des.*, 2009, **9**, 633.

5 S. Manna, K. Das and S. K. De, *ACS. Appl. Mater. Interfaces*, 2010, **2**, 1536.

6 N. Prabhakar, T. Nareoja, E. von Haartman, D. Sen Karaman, H. Jiang, S. Koho, T. A. Dolenko, P. E. Hanninen, D. I. Vlasov, V. G. Ralchenko, S. Hosomi, I. I. Vlasov, C. Sahlgren and J. M. Rosenholm, *Nanoscale*, 2013, **5**, 3713.

7 C. M. A. Parlett, K. Wilson and A. F. Lee, *Chem. Soc. Rev.*, 2013, **42**, 3876.

8 Z. Zhang, H. Che, Y. Wang, J. Gao, L. Zhao, X. She, J. Sun, P. Gunawan, Z. Zhong and F. Su, *Ind. Eng. Chem. Res.*, 2012, **51**, 1264.

9 F. X. Zhang, A. Yamakata, K. Maeda, Y. Moriya, T. Takata, J. Kubota, K. Teshima, S. Oishi and K. Domen, *J. Am. Chem. Soc.*, 2012, **134**, 8348.

10 C. Merlet, B. Rotenberg, P. A. Madden, P. L. Taberna, P. Simon, Y. Gogotsi and M. Salanne, *Nat. Mater.*, 2012, **11**, 306.

11 H. E. Wang, L. X. Zheng, C. P. Liu, Y. K. Liu, C. Y. Luan, H. Cheng, Y. Y. Li, L. Martinu, J. A. Zapien and I. Bello, *J. Phys. Chem. C*, 2011, **115**, 10419.

12 Y. H. Xu, Y. J. Zhu, Y. H. Liu and C. S. Wang, *Adv. Energy Mater.*, 2013, **3**, 128.

13 W. H. Ryu, J. Shin, J. W. Jung and I. D. Kim, *J. Mater. Chem. A*, 2013, **1**, 3239.

14 N. Yan, F. Wang, H. Zhong, Y. Li, Y. Wang, L. Hu and Q. W. Chen, *Sci. Rep.*, 2013, **3**, 1568.

15 Z. Zhang, H. Che, Y. Wang, L. Song, Z. Zhong and F. Su, *Catal. Sci. Technol.*, 2012, **2**, 1953.

16 B. O'Regan, D. T. Schwartz, S. M. Zakeeruddin and M. Gratzel, *Adv. Mater.*, 2000, **12**, 1263.

17 J. Jiang, J. P. Liu, R. M. Ding, X. X. Ji, Y. Y. Hu, X. Li, A. Z. Hu, F. Wu, Z. H. Zhu and X. T. Huang, *J. Phys. Chem. C*, 2010, **114**, 929.

18 C. Z. Yuan, L. Yang, L. R. Hou, L. F. Shen, X. G. Zhang and X. W. Lou, *Energy Environ. Sci.*, 2012, **5**, 7883.

19 A. Paravannoor, R. Ranjusha, A. M. Asha, R. Vani, S. Kalluri, K. R. V. Subramanian, N. Sivakumar, T. N. Kim, S. V. Nair and A. Balakrishnan, *Chem. Eng. J.*, 2013, **220**, 360.

20 X. Xu, R. Cao, S. Jeong and J. Cho, *Nano Lett.*, 2012, **12**, 4988.

21 Y. Ren, A. R. Armstrong, F. Jiao and P. G. Bruce, *J. Am. Chem. Soc.*, 2010, **132**, 996.

22 Z. Zhang, Y. Wang, Q. Tan, Z. Zhong and F. Su, *J. Colloid Interf. Sci.*, 2013, **398**, 185.

23 P. Lavela and J. L. Tirado, *J. Power Sources*, 2007, **172**, 379.

24 W. Luo, X. L. Hu, Y. M. Sun and Y. H. Huang, *J. Mater. Chem.*, 2012, **22**, 8916.

25 L. Hu, H. Zhong, X. R. Zheng, Y. M. Huang, P. Zhang and Q. W. Chen, *Sci. Rep.*, 2012, **2**, 1622.

26 C. Z. Yuan, J. Y. Li, L. R. Hou, X. G. Zhang, L. F. Shen and X. W. Lou, *Adv. Funct. Mater.*, 2012, **22**, 4592.

27 P. Lavela, N. A. Kyeremateng and J. L. Tirado, *Mater. Chem. Phys.*, 2010, **124**, 102.

28 M. Ghosh, G. Lawes, A. Gayen, G. N. Subbanna, W. M. Reiff, M. A. Subramanian, A. P. Ramirez, J. P. Zhang and R. Seshadri, *Chem. Mater.*, 2004, **16**, 118.

29 P. Z. Guo, L. J. Cui, Y. Q. Wang, M. Lv, B. Y. Wang and X. S. Zhao, *Langmuir*, 2013, **29**, 8997.

30 T. P. Braga, B. M. C. Sales, A. N. Pinheiro, W. T. Herrera, E. Baggio-Saitovitch and A. Valentini, *Catal. Sci. Technol.*, 2011, **1**, 1383.

31 A. B. Fuertes, T. Valdes-Solis, M. Sevilla and P. Tartaj, *J. Phys. Chem. C*, 2008, **112**, 3648.

32 Y. Y. Liang, H. L. Wang, P. Diao, W. Chang, G. S. Hong, Y. G. Li, M. Gong, L. M. Xie, J. G. Zhou, J. Wang, T. Z. Regier, F. Wei and H. J. Dai, *J. Am. Chem. Soc.*, 2012, **134**, 15849.

33 Y. Y. Liang, H. L. Wang, J. G. Zhou, Y. G. Li, J. Wang, T. Regier and H. J. Dai, *J. Am. Chem. Soc.*, 2012, **134**, 3517.

34 Y. Y. Liang, Y. G. Li, H. L. Wang, J. G. Zhou, J. Wang, T. Regier and H. J. Dai, *Nat. Mater.*, 2011, **10**, 780.

35 Z. Zhang, H. Chen, X. She, J. Sun, J. Teo and F. Su, *J. Power Sources*, 2012, **217**, 336.

36 X. J. Zhang, W. H. Shi, J. X. Zhu, W. Y. Zhao, J. Ma, S. Mhaisalkar, T. L. Maria, Y. H. Yang, H. Zhang, H. H. Hng and Q. Y. Yan, *Nano Res.*, 2010, **3**, 643.

37 L. Yu, G. Q. Zhang, C. Z. Yuan and X. W. Lou, *Chem. Commun.*, 2013, **49**, 137.

38 L. Zhou, D. Zhao and X. W. Lou, *Adv. Mater.*, 2012, **24**, 745.

39 G. Q. Zhang and X. W. Lou, *Sci. Rep.*, 2013, **3**, 1470

40 Y. L. Liu and A. R. H. Walker, *Angew. Chem. Int. Ed.*, 2010, **49**, 6781.

41 J. Luo, L. Han, N. N. Kariuki, L. Y. Wang, D. Mott, C. J. Zhong and T. He, *Chem. Mater.*, 2005, **17**, 5282.

42 J. Nai, Y. Tian, X. Guan and L. Guo, *J. Am. Chem. Soc.*, 2013, **135**, 16082.

43 X. Wang, J. Zhuang, Q. Peng and Y. D. Li, *Nature*, 2005, **437**, 121.

44 J. Yang and J. Y. Ying, *Nat. Mater.*, 2009, **8**, 683.

45 Z. Y. Zeng, T. Sun, J. X. Zhu, X. Huang, Z. Y. Yin, G. Lu, Z. X. Fan, Q. Y. Yan, H. H. Hng and H. Zhang, *Angew. Chem. Int. Ed.*, 2012, **51**, 9052.

46 Z. Jin, M. D. Xiao, Z. H. Bao, P. Wang and J. F. Wang, *Angew. Chem. Int. Ed.*, 2012, **51**, 6406.

47 L. Z. Wang, F. Q. Tang, K. Ozawa, Z. G. Chen, A. Mukherj, Y. C. Zhu, J. Zou, H. M. Cheng and G. Q. Lu, *Angew. Chem. Int. Ed.*, 2009, **48**, 7048.

48 H. Liu, J. L. Qu, Y. F. Chen, J. Q. Li, F. Ye, J. Y. Lee and J. Yang, *J. Am. Chem. Soc.*, 2012, **134**, 11602.

49 C. C. Li and H. C. Zeng, *J. Am. Chem. Soc.*, 2012, **134**, 19084.

50 J. Zhang and J. Y. Fang, *J. Am. Chem. Soc.*, 2009, **131**, 18543.

51 G. Q. Zhang, B. Y. Xia, C. Xiao, L. Yu, X. Wang, Y. Xie and X. W. Lou, *Angew. Chem. Int. Ed.*, 2013, **52**, 8643.

52 L. Zhou, C. Gao, X. Z. Hu and W. J. Xu, *Chem. Mater.*, 2011, **23**, 1461.

53 H. G. Wang, D. L. Ma, X. L. Huang, Y. Huang and X. B. Zhang, *Sci. Rep.*, 2012, **2**, 701.

54 Y. P. Du, Z. Y. Yin, J. X. Zhu, X. Huang, X. J. Wu, Z. Y. Zeng, Q. Y. Yan and H. Zhang, *Nat. Commun.*, 2012, **3**, 1177.

55 X. H. Liu, R. Z. Ma, Y. Bando and T. Sasaki, *Adv. Mater.*, 2012, **24**, 2148.

56 X. Y. Lai, J. Li, B. A. Korgel, Z. H. Dong, Z. M. Li, F. B. Su, J. A. Du and D. Wang, *Angew. Chem. Int. Ed.*, 2011, **50**, 2738.

57 Z. Zhang, H. Che, Y. Wang, J. Gao, X. She, J. Sun, Z. Zhong and F. Su, *RSC Adv.*, 2012, **2**, 2254.

58 Z. Zhang, Y. Wang, M. Zhang, Q. Tan, X. Lv, Z. Zhong and F. Su, *J. Mater. Chem. A*, 2013, **1**, 7444.

59 K. Verma, A. Kumar and D. Varshney, *J. Alloys Compd.*, 2012, **526**, 91.

60 X. M. Liu and S. Y. Fu, *J. Magn. Magn. Mater.*, 2007, **308**, 61.

61 A. Daigle, J. Modest, A. L. Geiler, S. Gillette, Y. Chen, M. Geiler, B. Hu, S. Kim, K. Stopher, C. Vittoria and V. G. Harris, *Nanotechnology*, 2011, **22**, 30.

62 C. S. Hwang and N. C. Wang, *Mater. Chem. Phys.*, 2004, **88**, 258.

63 K. Maaz, S. Karim, K. J. Lee, M. H. Jung and G. H. Kim, *Mater. Chem. Phys.*, 2012, **133**, 1006.

64 Z. Zhang, Y. Wang, D. Li, Q. Tan, Y. Chen, Z. Zhong and F. Su, *Ind. Eng. Chem. Res.*, 2013, **52**, 14906.

65 L. Zhang, H. B. Wu, S. Madhavi, H. H. Hng and X. W. Lou, *J. Am. Chem. Soc.*, 2012, **134**, 17388.

66 P. Lavela, J. L. Tirado, M. Womes and J. C. Jumas, *J. Electrochem. Soc.*, 2009, **156**, A589.

67 R. Tummala, R. K. Guduru and P. S. Mohanty, *J. Power Sources*, 2012, **199**, 270.

68 N. Du, Y. F. Xu, H. Zhang, J. X. Yu, C. X. Zhai and D. R. Yang, *Inorg. Chem.*, 2011, **50**, 3320.

List of Table

Table 1: The synthesis conditions used for prepared MTMOs mesoporous nanospheres.

Figure Captions:

Fig. 1 SEM images (first and third column), TEM images (second and fourth column) of the ternary $Zn_{0.5}Co_{0.5}Fe_2O_4$ (a and b), $Zn_{0.5}Mn_{0.5}Fe_2O_4$ (c and d), $Zn_{0.5}Ni_{0.5}Fe_2O_4$ (e and f), $Ni_{0.5}Mn_{0.5}Fe_2O_4$ (g and h), $Ni_{0.5}Co_{0.5}Fe_2O_4$ (i and j), and $Mn_{0.5}Co_{0.5}Fe_2O_4$ (k and l).

Fig. 2 SEM images (a, d, g, j, and m), TEM images (b, e, h, k, and n), and HRTEM images (c, f, i, l, and of the quaternary $Zn_{0.33}Ni_{0.33}Mn_{0.33}Fe_2O_4$ mesoporous nanospheres of (a, b, and c), $Ni_{0.33}Mn_{0.33}Co_{0.33}Fe_2O_4$ (d, e, and f), $Zn_{0.33}Mn_{0.33}Co_{0.33}Fe_2O_4$ (g, h, and i), $Zn_{0.33}Ni_{0.33}Co_{0.33}Fe_2O_4$ (j, k, and l) and the pentabasic $Zn_{0.25}Ni_{0.25}Mn_{0.25}Co_{0.25}Fe_2O_4$ (m, n, and 0). (Inset of Fig. 2i and 2o are the selected-area electron diffraction (SAED) patterns of $Zn_{0.33}Ni_{0.33}Co_{0.33}Fe_2O_4$ and $Zn_{0.25}Ni_{0.25}Mn_{0.25}Co_{0.25}Fe_2O_4$ mesoporous nanospheres.)

Fig. 3 STEM image and elemental mappings of $Zn_{0.5}Co_{0.5}Fe_2O_4$ (a) and $Ni_{0.33}Mn_{0.33}Co_{0.33}Fe_2O_4$ (b).

Fig. 4 Electrochemical properties: the first and second discharge-charge curves of $Ni_{0.5}Mn_{0.5}Fe_2O_4$ (a) and $Ni_{0.33}Mn_{0.33}Co_{0.33}Fe_2O_4$ (b), cycling performance and coulombic efficiency of $Ni_{0.5}Mn_{0.5}Fe_2O_4$ and $Ni_{0.33}Mn_{0.33}Co_{0.33}Fe_2O_4$ at a current density of 50 mA g^{-1} (c), and CV curves of $Ni_{0.5}Mn_{0.5}Fe_2O_4$ at a scan rate of 0.1 mV s^{-1} (d).

Table 1: The synthesis conditions used for prepared MTMOs mesoporous nanospheres.

Entry	Sample	$FeCl_3$ (mmol)	$Co(CH_3COO)_2$ (mmol)	$Mn(CH_3COO)_2$ (mmol)	$Ni(CH_3COO)_2$ (mmol)	$Zn(CH_3COO)_2$ (mmol)	CH_3COONa (mmol)	$HOCH_2CH_2OH$ (ml)	H_2O (ml)
1	Fe_2O_3	2.0					18	80	
2	CoO		2.0				18	80	
3	ZnO					2.0	18	80	
4	NiO				2.0		18	80	
5	MnO			2.0			18	80	
6	$CoFe_2O_4$	2.0	1.0				18	80	
7	$NiFe_2O_4$	2.0			1.0		18	80	
8	$MnFe_2O_4$	2.0		1.0			18	80	
9	$ZnFe_2O_4$	2.0				1.0	18	80	
10	$Zn_{0.2}Co_{0.8}Fe_2O_4$	2.0	0.8			0.2	18	80	
11	$Zn_{0.8}Co_{0.2}Fe_2O_4$	2.0	0.2			0.8	18	80	
12	$Zn_{0.5}Co_{0.5}Fe_2O_4$	2.0	0.5			0.5	18	80	
13	$Zn_{0.5}Co_{0.5}Fe_2O_4$	2.0	0.5			0.5	12	80	
14	$Zn_{0.5}Co_{0.5}Fe_2O_4$	2.0	0.5			0.5	9	80	
15	$Zn_{0.5}Co_{0.5}Fe_2O_4$	2.0	0.5			0.5	6	80	
16	$Zn_{0.5}Co_{0.5}Fe_2O_4$	2.0	0.5			0.5	3	80	
17	$Zn_{0.5}Co_{0.5}Fe_2O_4$	2.0	0.5			0.5	0	80	
18	$Zn_{0.5}Co_{0.5}Fe_2O_4$	2.0	0.5			0.5	18	70	10
19	$Zn_{0.5}Co_{0.5}Fe_2O_4$	2.0	0.5			0.5	18	60	20
20	$Zn_{0.5}Co_{0.5}Fe_2O_4$	2.0	0.5			0.5	18	50	30
21	$Zn_{0.5}Co_{0.5}Fe_2O_4$	2.0	0.5			0.5	18	40	40
22	$Ni_{0.5}Mn_{0.5}Fe_2O_4$	2.0		0.5	0.5		18	80	
23	$Zn_{0.5}Mn_{0.5}Fe_2O_4$	2.0		0.5		0.5	18	80	
24	$Zn_{0.5}Ni_{0.5}Fe_2O_4$	2.0			0.5	0.5	18	80	
25	$Mn_{0.5}Co_{0.5}Fe_2O_4$	2.0	0.5	0.5			18	80	
26	$Ni_{0.5}Co_{0.5}Fe_2O_4$	2.0	0.5		0.5		18	80	
27	$Zn_{0.2}Ni_{0.4}Mn_{0.4}Fe_2O_4$	2.0		0.4	0.4	0.2	18	80	
28	$Zn_{0.4}Ni_{0.2}Mn_{0.4}Fe_2O_4$	2.0		0.4	0.2	0.4	18	80	
29	$Zn_{0.33}Ni_{0.33}Mn_{0.33}Fe_2O_4$	2.0		0.33	0.33	0.33	18	80	
30	$Ni_{0.33}Mn_{0.33}Co_{0.33}Fe_2O_4$	2.0	0.33	0.33	0.33		18	80	
31	$Zn_{0.33}Mn_{0.33}Co_{0.33}Fe_2O_4$	2.0	0.33	0.33		0.33	18	80	
32	$Zn_{0.33}Ni_{0.33}Co_{0.33}Fe_2O_4$	2.0	0.33		0.33	0.33	18	80	
33	$Zn_{0.25}Ni_{0.25}Mn_{0.25}Co_{0.25}Fe_2O_4$	2.0	0.25	0.25	0.25	0.25	18	80	
34	$Zn_{0.5}Ni_{0.5}Mn_2O_4$			2.0	0.5	0.5	18	80	
35	$Zn_{0.33}Ni_{0.33}Mn_{0.33}Co_2O_4$		2.0	0.33	0.33	0.33	18	80	

List of Figures:

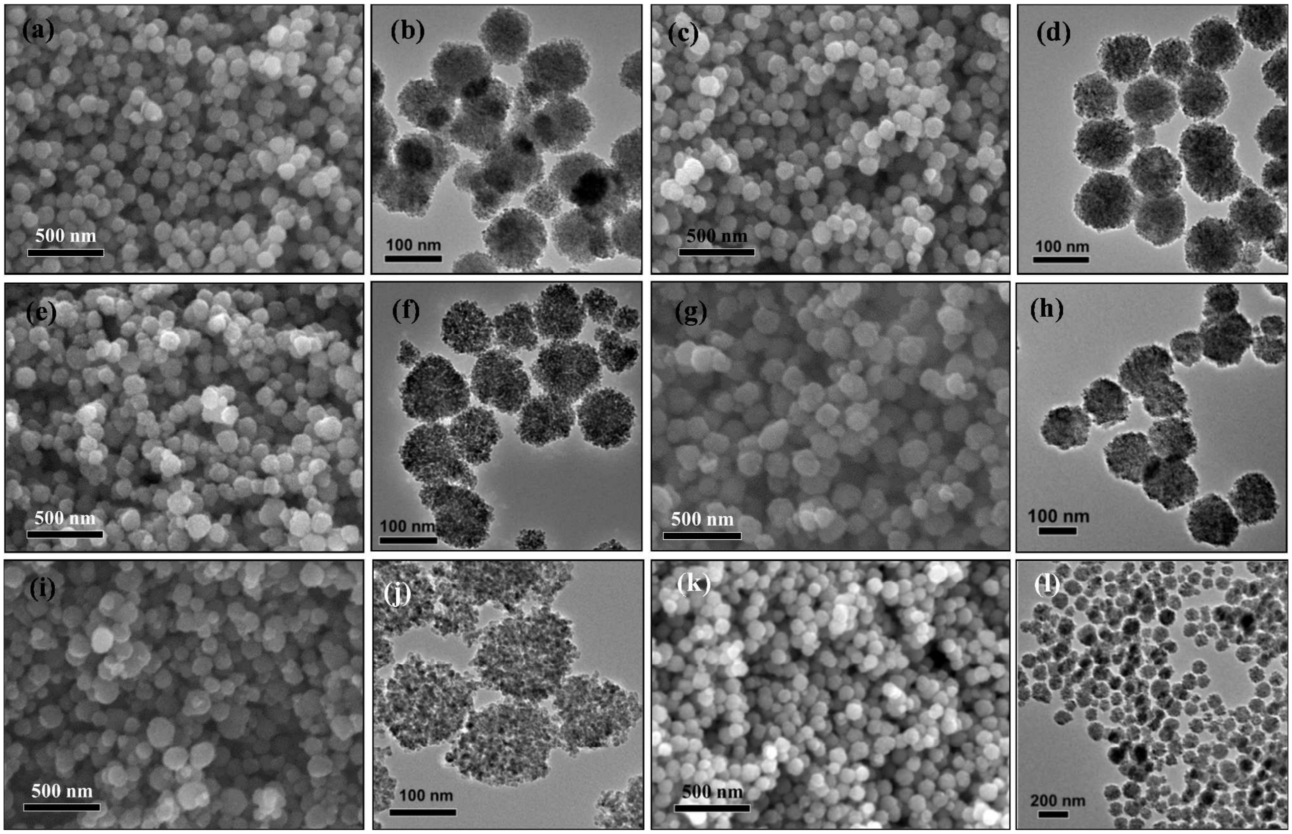

Fig. 1

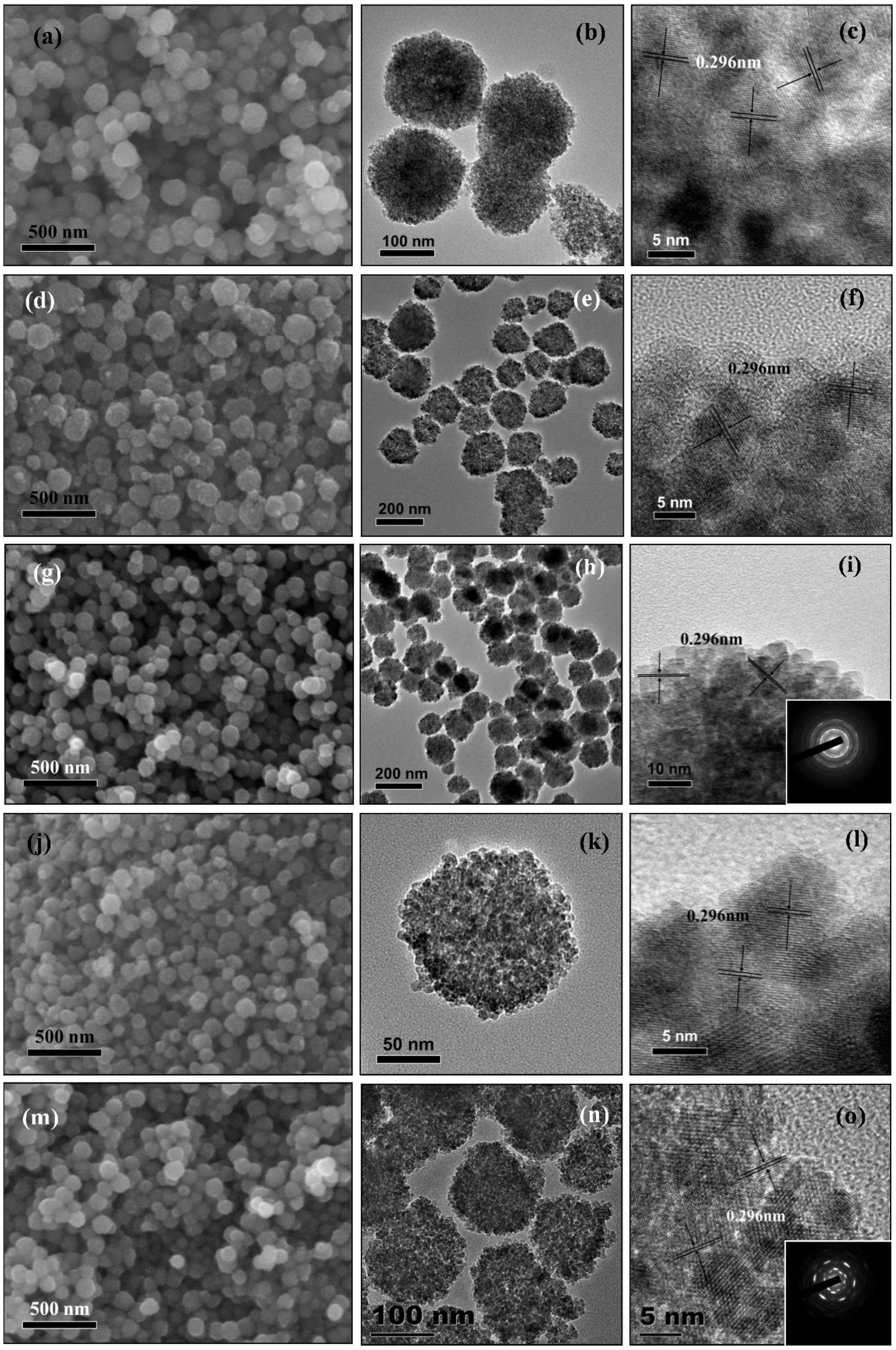
(a)
500 nm
(b)
100 nm
(c)
0.296nm
5 nm
(d)
500 nm
(e)
200 nm
(f)
0.296nm
5 nm
(g)
500 nm
(h)
200 nm
(i)
0.296nm
10 nm
(j)
500 nm
(k)
50 nm
(l)
0.296nm
5 nm
(m)
500 nm
(n)
100 nm
(o)
0.296nm
5 nm

Fig. 2

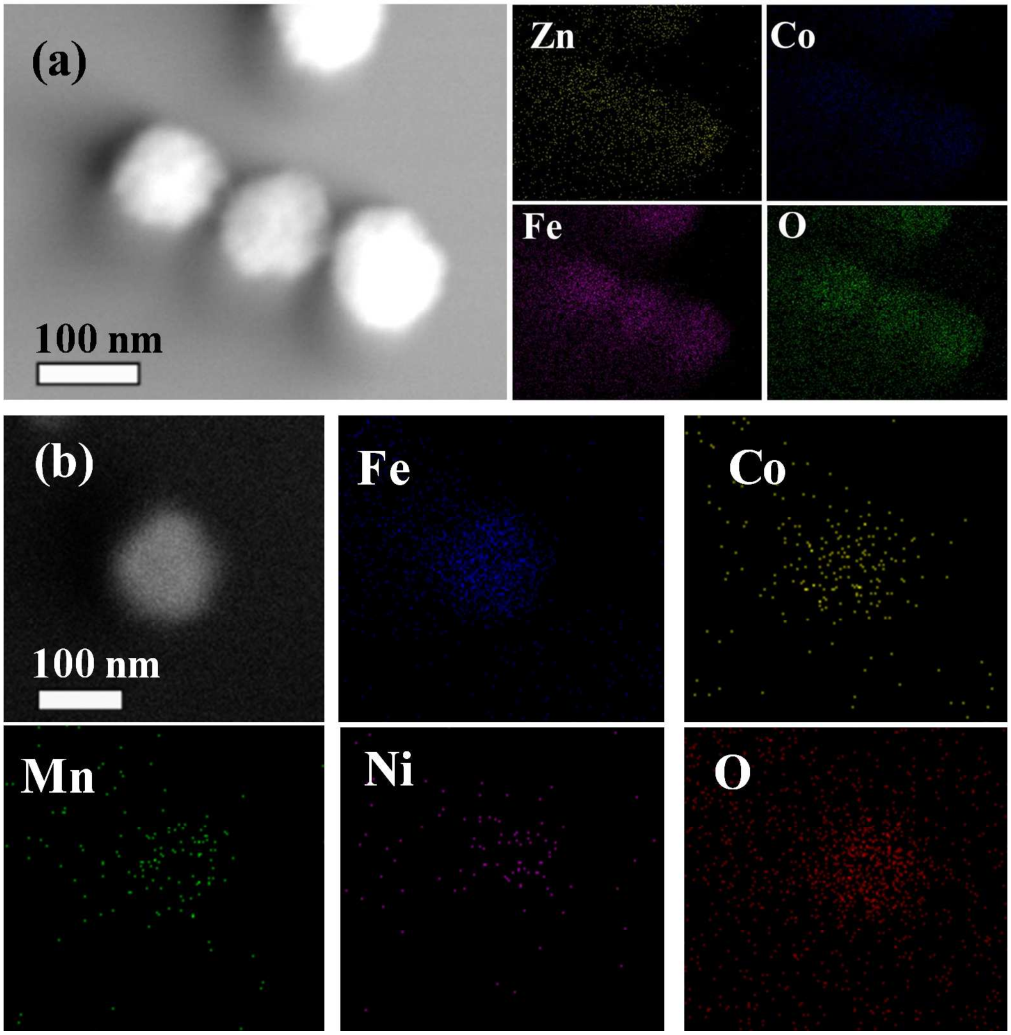

Fig. 3

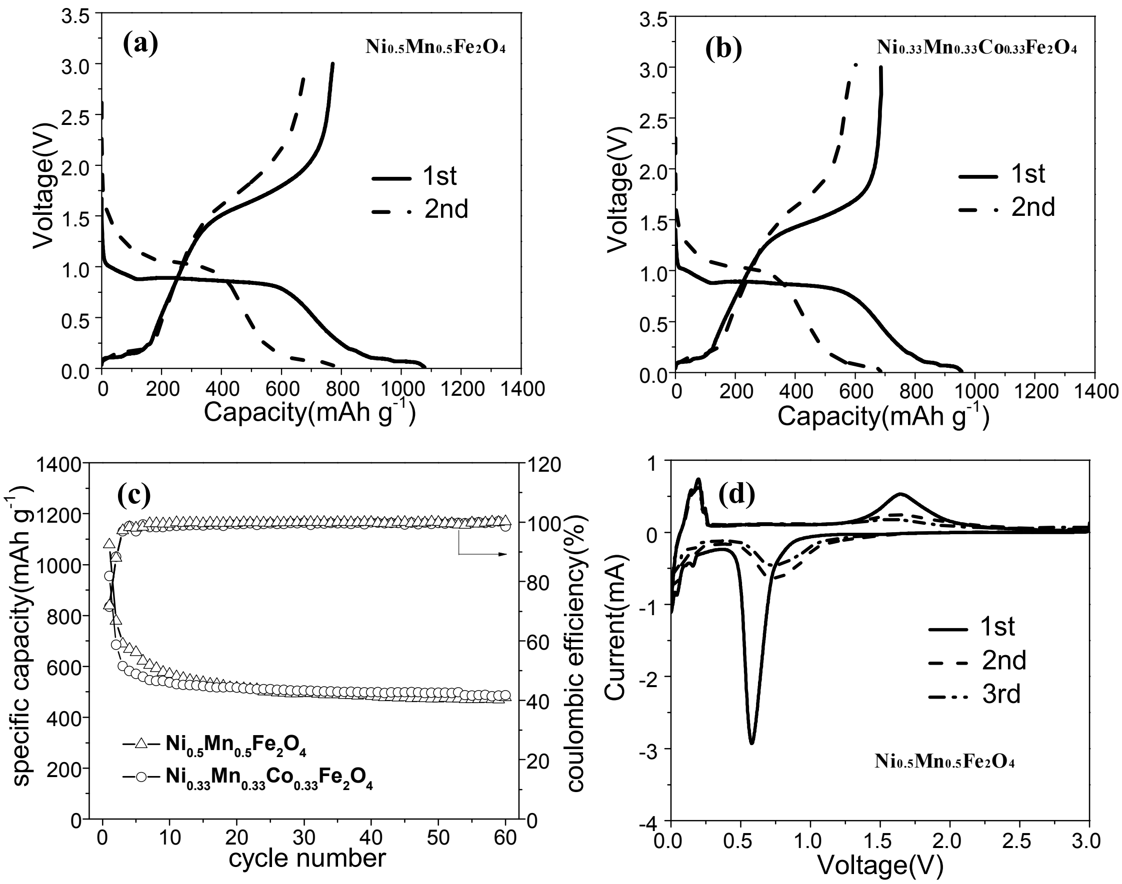
(a)
Ni0.5Mn0.5Fe2O4
1st
2nd
Voltage(V)
Capacity(mAh g-1)
(b)
Ni0.33Mn0.33Co0.33Fe2O4
1st
2nd
Voltage(V)
Capacity(mAh g-1)
(c)
specific capacity(mAh g-1)
coulombic efficiency(%)
Ni0.5Mn0.5Fe2O4
Ni0.33Mn0.33Co0.33Fe2O4
cycle number
(d)
1st
2nd
3rd
Ni0.5Mn0.5Fe2O4
Current(mA)
Voltage(V)

Fig. 4

Graphic Abstract

A general approach has been developed for the fabrication of multiple transition metal oxides mesoporous nanospheres with controllable composition.